Article

Effects of Fluorination and Molybdenum Codoping on Monoclinic BiVO$_4$ Photocatalyst by HSE Calculations

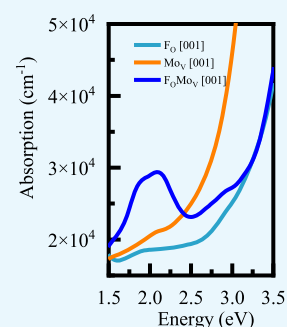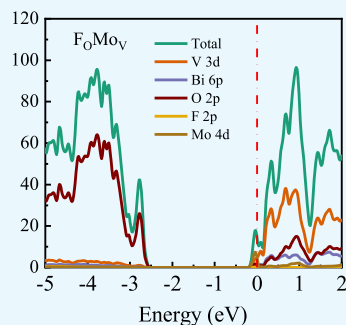Xia Chen,[⊥] Yonggang Wu,[⊥] MingSen Deng, Hujun Shen, Jianwen Ding,* and Wentao Wang*

Read Online

ACCESS | Metrics & More | Article Recommendations

ABSTRACT: Monoclinic phase bismuth vanadate (BiVO$_4$) is one of the most promising photoelectrochemical materials used in water-splitting photoelectrochemical cells. It could be even better if its band gap and charge transport characteristics were optimized. Although codoping of BiVO$_4$ has proven to be an effective strategy, its effects are remarkably poorly understood. Using the Heyd−Scuseria−Ernzerhof (HSE) hybrid functional, we estimate the formation energy, electronic properties, and photocatalytic activities of F and Mo codoped BiVO$_4$. We find that Mo atoms prefer to replace V atoms, whereas F atoms prefer to replace O atoms (F$_O$Mo$_V$-doped BiVO$_4$) under oxygen-poor conditions according to calculated formation energies. BiVO$_4$ doped with F$_O$Mo$_V$ is found to be shallow-level doped, occurring with some continuum states above the conduction band edge, which is advantageous for photochemical catalysis. Moreover, F$_O$Mo$_V$-doped BiVO$_4$ shows absorption stronger than that of pure BiVO$_4$ in the visible spectrum. Based on the band-edge calculation, BiVO$_4$ doped with F$_O$Mo$_V$ still retains a high oxidizing capacity. It has been shown that F$_O$Mo$_V$-doped BiVO$_4$ exhibits a very high photocatalytic activity under visible light.

1. INTRODUCTION

In 1999, Kudo et al.[1] reported monoclinic phase bismuth vanadate (BiVO$_4$) as a photocatalyst to achieve water oxidation. They used Ag$^+$ ions as an electron scavenger under visible light irradiation. Since then, BiVO$_4$ has gradually been a hot research topic because of its great potential in energy conversion and the environmental field. However, the wide application of BiVO$_4$ is still limited. This is due to its low electron transfer efficiency,[2] slow water oxidation kinetics,[3] poor charge carrier mobility,[4] and weak surface adsorption capacity.[5] Therefore, various modification strategies have enhanced photocatalytic performance in the past few years. These strategies included morphological modification,[6] crystal facet control,[7] semiconductor coupling,[8,9] deposition of cocatalysts,[10] element doping,[11] and defect formation.[12]

Among the above strategies, the doping of pure BiVO$_4$ with either anions or cations remains one of the most common methods used to increase carrier density and reduce charge transfer resistance. For cation doping, notably, Mo doping could effectively modulate the electronic structure of BiVO$_4$, leading to both increased carrier concentration and improved optical absorption.[13] For example, Yang et al. synthesized a high-quality Mo-doped BiVO$_4$ photoanode using a simple drop-casting method.[14] The results revealed that Mo-doped BiVO$_4$ produced a much higher photocurrent than undoped BiVO$_4$ under AM 1.5G illumination for water oxidation. For anion doping, it has been widely adopted to improve the electrochemical properties of BiVO$_4$. Experimentally, a F-doped BiVO$_4$ photocatalyst is synthesized by a simple two-step hydrothermal process.[15] It is found that the substitution of O by F could result in the decrease of the BiVO$_4$ lattice parameters, influence the chemical environment surrounding the Bi, V, and O elements, cause the red-shift of the adsorption edge, and modify the absorption abilities in the visible light region. More importantly, the anion−cation codoping has been an effective method to improve the photocatalytic effect. For instance, Rohloff et al. fabricated a F/Mo:BiVO$_4$ thin film photoanode via soft fluorination.[16] They demonstrated that anion and cation codoping in BiVO$_4$ allows combining the PEC-relevant benefits associated with each type of dopant, the increased conductivity and charge separation due to Mo doping, and the increased water oxidation catalysis efficiency introduced by fluorination. However, it is still unclear what exactly these promoting effects are. The F/Mo codoping effects on BiVO$_4$'s photocatalytic activity are still not entirely understood.

Theoretically, F- or Mo-doped $BiVO_4$ has been calculated with the generalized gradient approximation (GGA)[17] of the Perdew−Burke−Ernzerhof (PBE)[18] method (GGA-PBE) and GGA+U method. Ding et al.[19] calculated the band structure and density of states of F-doped $BiVO_4$. It was discovered that the doped F would act as electron capture traps that would benefit the separation of the photoinduced carriers and improve the photocatalytic performance of $BiVO_4$. Because of the difference in valence electrons between the F and O atoms, the F atom has one more. The substitution of an F atom for an O atom in $BiVO_4$ will increase the Fermi level by one electron. Our previous GGA+U study[11] for Mo-doped $BiVO_4$ indicated that the Mo 4d impurity states would be observed in the band gap when Mo is doped on the Bi lattice site. It is important to note that these impurities can easily trap carriers and lower carrier mobility, which can harm the application of Mo-doped $BiVO_4$ in the photoelectrochemical conversion of solar energy. There is no impurity state in the band gap while Mo is doping on the V lattice site. The band gap is smaller in this case, resulting in higher optical absorption. These results are the same as the other GGA method.[20] However, it is known that the GGA-PBE usually suffers from band gap underestimation.[21] Furthermore, the GGA+U correction was only applied to the d electrons of V and Mo, while the other components were treated within GGA. Thus, quantitatively more accurate calculations are necessary.

In this paper, based on the Heyd−Scuseria−Ernzerhof (HSE) hybrid functional, we calculate the formation energy, electronic properties, and photocatalytic activity of F and Mo codoped $BiVO_4$. According to calculated formation energies, Mo atoms prefer to replace V atoms, whereas F atoms prefer to replace O atoms ($F_O Mo_V$-doped $BiVO_4$) under oxygen-poor conditions. $BiVO_4$ doped with $F_O Mo_V$ is found to be shallow-level doped, with some continuum states occurring above the conduction band edge. Moreover, $F_O Mo_V$-doped $BiVO_4$ shows absorption stronger than that of pure $BiVO_4$ in the visible spectrum. Based on the band-edge calculation, $BiVO_4$ doped with $F_O Mo_V$ still retains a high oxidizing capacity. Thus, $F_O Mo_V$-doped $BiVO_4$ is particularly suitable for visible light photocatalysis. Our results provide more general design guidelines for the preparation of codoped $BiVO_4$ with the promise of further performance improvements.

2. COMPUTATIONAL DETAILS

A plane-wave projector-augmented wave (PAW) method[22] is used to perform all density functional theory calculations using the Vienna Ab initio Simulation Package (VASP).[23,24] A kinetic-energy cutoff of 500 eV is tested to be sufficient for plane-wave expansion to achieve good convergence. Electronic self-consistent interaction convergence is considered sufficient for a total energy difference of less than 10^{-5} eV, and the forces on each ion converged were less than 0.03 eV/Å. The positions of all atoms in the system are allowed to relax. The PAW potentials with the valence electrons $6s^2 6p^3$ for Bi, $3d^3 4s^2$ for V, $2s^2 2p^4$ for O, $2s^2 2p^5$ for F, and $4d^5 5s^1$ for Mo have been employed. We used the PBE exchange-correlation functional within the GGA[18] for geometry optimizations. Doping defect calculations are performed in a $2 \times 2 \times 1$ supercell. For these systems, we used $3 \times 3 \times 3$ Monkhorst−Pack k-point meshes,[25] which are found to be sufficient to reach convergence for bulk calculations and used for geometry optimization and electronic property calculations. It is well-

known that the PBE typically suffers from the underestimation of the band gap.[26,27] The HSE[28,29] functional can now provide more accurate band gap measurements than the GGA methods. Therefore, this paper obtains the electronic structures, the optical absorption coefficient, and electrostatic potential energy using the HSE functional. For the HSE hybrid functional, the screening parameter is set to 0.2 Å^{-1}, the Hartree−Fock mixing parameter is $\alpha = 0.15$. Using these HSE parameters, we calculated the band gap of pure $BiVO_4$ to be 2.4 eV, which is consistent with experiment (2.5 eV[30]) and the previous theoretical study (2.45 eV[8] and 2.58 eV[12]).

The defect formation energy is an essential measure of the stability for the F and/or Mo defects in $BiVO_4$, which is defined as

$$E_{form} = E_{def} - E_{pure} + \sum_i \mu_i \tag{1}$$

In the formula, E_{def} and E_{pure} are the total energies of supercells with a defect and a perfect supercell, respectively. The μ_i is the chemical potential of chemical species i (i = Bi, V, O, F, Mo). For Bi, V, and O in $BiVO_4$, chemical potentials are not arbitrary but are influenced by thermodynamic constraints that can represent actual experimental conditions. In our previous work, we calculated the phase diagram of $BiVO_4$ as a two-dimensional panel with three independent variables $\Delta\mu_{Bi}$, $\Delta\mu_V$, and $\Delta\mu_O$ by the HSE functional.[12] Thus, as shown in Figure S3 of ref 12, in this paper, we use representative chemical potential point A_{HSE} ($\Delta\mu_{Bi}$, $\Delta\mu_V$, $\Delta\mu_O$) = (−3.69, −8.27, 0) for the O-rich growth condition and D_{HSE} ($\Delta\mu_{Bi}$, $\Delta\mu_V$, $\Delta\mu_O$) = (0, −2.12, −2.46) for the O-poor growth condition. Due to $\mu_{Bi} = E_{Bi} + \Delta\mu_{Bi}$, $\mu_V = \Delta\mu_V - E_V$, $\mu_O = \Delta\mu_O + E_O$, the corresponding chemical potential (μ) limits for A_{HSE} (μ_{Bi}, μ_V, μ_O) = (−7.98, −18.0, −6.16) and D_{HSE} (μ_{Bi}, μ_V, μ_O) = (−4.29, −11.85, −8.62).

In order to avoid the formation of phases containing impurities, the chemical potential of the impurities must meet the constraints. For Mo and F doping, the chemical potential of Mo and F is constrained by

$$\Delta\mu_F < 0, \ \Delta\mu_{Mo} < 0 \tag{2}$$

$$\Delta\mu_{Mo} + 3\Delta\mu_O < \Delta H_f(MoO_3) \tag{3}$$

$$\Delta\mu_{Mo} + 6\Delta\mu_F < \Delta H_f(MoF_6) \tag{4}$$

$$\Delta\mu_{Bi} + 3\Delta\mu_O < \Delta H_f(BiF_3) \tag{5}$$

$$\Delta\mu_V + 2\Delta\mu_F < \Delta H_f(VF_2) \tag{6}$$

$$\Delta\mu_V + 5\Delta\mu_F < \Delta H_f(VF_5) \tag{7}$$

Table 1 summarizes the calculated formation energy (given per formula unit) for MoO_3, MoF_6, BiF_3, VF_2, and VF_5, together with available experimental data. It is found that the

Table 1. Formation Enthalpy (eV/formula unit) Calculated by HSE Functional Compared to Experimental Values[33]

	HSE	experiment
$\Delta H_f(MoO_3)$	−6.80	−7.76
$\Delta H_f(MoF_6)$	−16.58	−17.65
$\Delta H_f(BiF_3)$	−9.90	−9.41
$\Delta H_f(VF_2)$	−6.95	−8.72
$\Delta H_f(VF_5)$	−16.23	−14.60

HSE calculations produce similar results, and the calculated values agree with the experimental values. HSE total energy calculations are performed using experimental lattice constants for MoO_3, MoF_6, BiF_3, VF_2, and VF_5. Table 2 lists these lattice

Table 2. Experimental Lattice Constants of MoO_3, MoF_6, BiF_3, VF_2, and VF_5 Used for the HSE Functional Total Energy Calculations[a]

	k-points	space group	experiment
MoO_3	$8 \times 3 \times 10$	Pbmn	$a = 3.964$, $b = 13.863$, $c = 3.699$; $\alpha = 90$, $\beta = 90$, $\gamma = 90$[34]
MoF_6	$3 \times 4 \times 6$	Pnma	$a = 9.480$, $b = 8.600$, $c = 4.993$; $\alpha = 90$, $\beta = 90$, $\gamma = 90$[35]
BiF_3	$5 \times 5 \times 5$	Pm3m	$a = 5.861$, $b = 5.861$, $c = 5.861$; $\alpha = 90$, $\beta = 90$, $\gamma = 90$[36]
VF_2	$6 \times 6 \times 9$	$P4_2/mnm$	$a = 4.804$, $b = 4.804$, $c = 3.236$; $\alpha = 90$, $\beta = 90$, $\gamma = 90$[37]
VF_5	$6 \times 2 \times 4$	Pmcn	$a = 5.4$, $b = 16.72$, $c = 7.53$; $\alpha = 90$, $\beta = 90$, $\gamma = 90$[38]

[a]Values a, b, and c are in angstroms, and the values α, β, and γ are in degrees.

constants. The following calculations use maximum Mo and F chemical potential that satisfies these inequations.[31,32] Under the O-rich growth condition, Mo and F chemical potentials are -18.86 and -4.71 eV, respectively, whereas under the O-poor growth condition, Mo and F chemical potentials are -11.48 and -5.94 eV, respectively. We use these chemical potentials to calculate formation energy for Mo- and F-related defects.

3. RESULTS AND DISCUSSION

3.1. Doped Configuration and Formation Energies.
Because the $I2/b$ space group is easily related to the tetragonal scheelite structure for pure $BiVO_4$, we chose to use it.[39] We used two $BiVO_4$ units (primitive units) to determine the structure through careful optimization of volume and relaxation of atomic positions. The optimization parameters are as follows: $a = 5.1556$ Å, $b = 5.0958$ Å, $c = 11.6067$ Å, and γ

= 90.2416°. There is good agreement between these lattice parameters and experimental values.[40] The results indicate that our calculation methods are accurate, while the calculated results are legitimate. In order to dope the structures, we used the $2 \times 2 \times 1$ supercell of monoclinic $BiVO_4$ (Figure 1a), which contains 64 oxygen atoms and 16 bismuth atoms. The doping concentration is about 1–2 atom %, consistent with the experimental results.[16] In order to introduce impurity atoms into the supercell, we use the modes F_O (F atoms substituting for O atoms in the lattice, Figure 1b), Mo_{Bi} (Mo atoms substituting for the Bi atoms in the lattice, Figure 1c), and Mo_V (Mo atoms substituting for V atoms in the lattice, Figure 1d), resulting in two different modes of F/Mo codoped monoclinic $BiVO_4$ models F_OMo_{Bi}-$BiVO_4$ (Figure 1e) and F_OMo_V-$BiVO_4$ (Figure 1f).

Table 3 lists the formation energies for F and Mo monodoped and F/Mo codoped $BiVO_4$ under O-poor and

Table 3. Formation Energies (eV) for F and Mo Monodoped and F/Mo Codoped $BiVO_4$

doped $BiVO_4$	O-poor	O-rich
F_O	0.75	1.98
Mo_{Bi}	1.77	5.46
Mo_V	0.22	1.45
F_OMo_{Bi}	2.19	7.11
F_OMo_V	0.75	3.21

O-rich growth conditions. It can be seen from Table 3 that the formation energies under the oxygen-poor condition are smaller than those of the oxygen-rich condition, which is consistent with the previous theoretical calculation.[31] This result implies that the oxygen-poor condition should always be used, whether cation site doping or anion site doping. Under the O-poor growth condition, the formation energy of F_O is 0.75 eV, which is close to 0 eV. This result suggests that the F doping on the O site in $BiVO_4$ is realized experimentally.[15,41,42] Under the O-poor and O-rich growth conditions, the
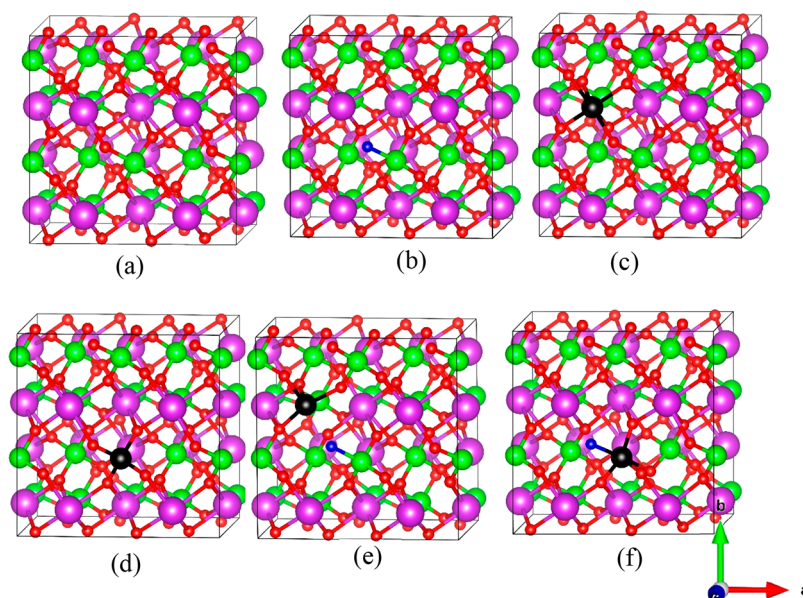

Figure 1. Doping structures of $BiVO_4$ after geometry optimization. (a) Pure $BiVO_4$, (b) F_O, (c) Mo_{Bi}, (d) Mo_V, (e) F_OMo_{Bi}, and (f) F_OMo_V-doped $BiVO_4$. The purple, green, red, black and blue spheres represent Bi, V, O, Mo and F atoms, respectively.

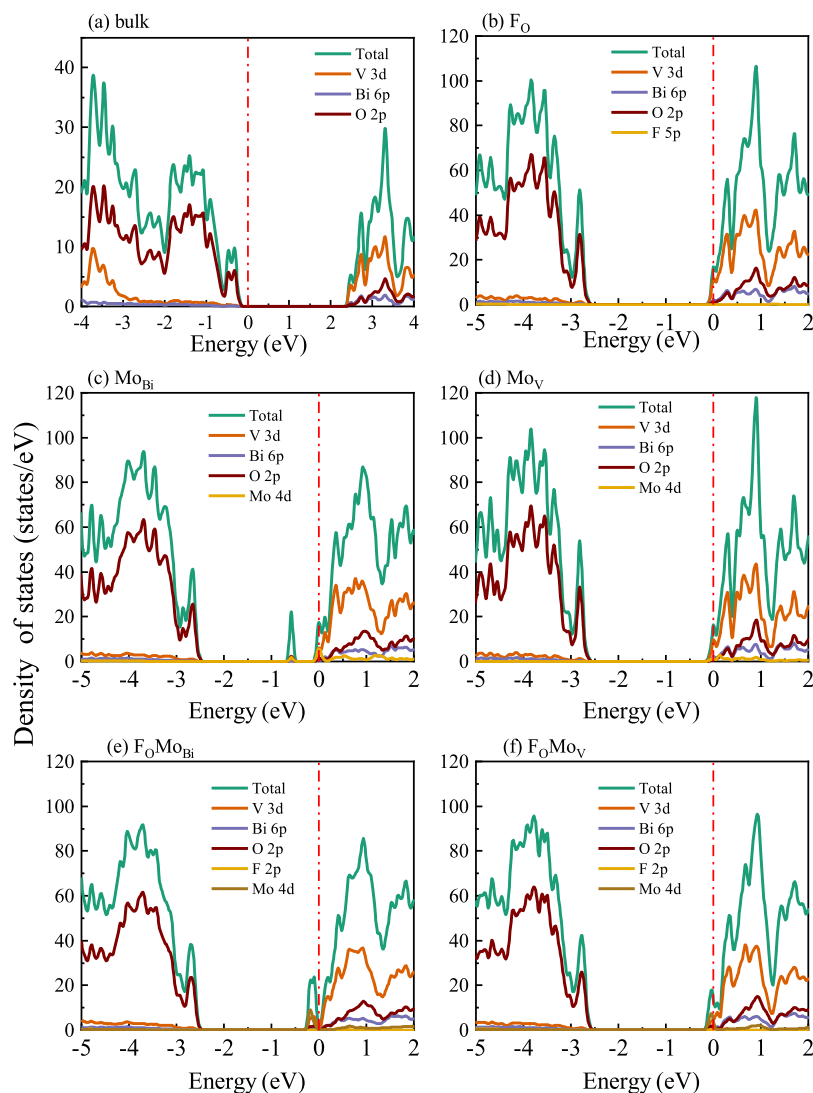**Figure 2.** Total density of states and partial density of states for (a) bulk $BiVO_4$ and (b) F_O, (c)Mo_{Bi}, (d)Mo_V, (e) F_OMo_{Bi}, and (f) F_OMo_V-doped $BiVO_4$. The red dot-dash lines denote the Fermi level.

formation energies of Mo_V are smaller than those of Mo_{Bi}. This means the Mo atom prefers to substitute the V atom, consistent with the experimental[43] and theoretical[11,31] results. This has resulted in the formation energies of F_OMo_V being smaller than those of F_OMo_{Bi}. This result suggests that the F/Mo codoped $BiVO_4$ is much easier to form F_OMo_V-$BiVO_4$,[16] and F_OMo_{Bi}-$BiVO_4$ is generally hard to obtain experimentally.

3.2. Electronic Structures. Figure 2 shows the total density of states (TDOS) and partial density of states (PDOS) of F_O, Mo_{Bi}, Mo_V, F_OMo_{Bi}, and F_OMo_V-doped $BiVO_4$ between −5 and 2 eV based on the HSE function. Additionally, the electronic properties of pure $BiVO_4$ are also calculated in order to compare the F- and Mo-doped $BiVO_4$. As shown in Figure 2a, the band gap of pure $BiVO_4$ is 2.40 eV, consistent with the experimental data (2.50 eV)[30] and theoretical results.[8,12]

For F_O-doped $BiVO_4$, the Fermi level is located at the top of the conduction band, as shown in Figure 2b. It is a typical n-type doping as the F atom has one more p electron than does the O atom. The band gap is 2.3 eV, similar to that of pure $BiVO_4$, which is in excellent agreement with the experimental results.[15,41] The partial charge density at the conduction band minimum (CBM) is shown in Figure 3a. This implies shallow-

level doping as the wave function is delocalized. The reason for this is that shallow levels have delocalized wave functions, whereas deep levels have localized ones.[31] Figure 2c shows the TDOS and PDOS of Mo_{Bi}-doped $BiVO_4$. There is an occupied state in the band gap at −0.45 to −0.71 eV below the Fermi energy. This occupied surface state is primarily dominated by O 2p, V 3d, and Mo 4d states. In the absence of occupied states, the band gap is 2.25 eV. This is evident in Figure 3b, which shows the partial charge density in the energy range between −0.45 and −0.71 eV below the Fermi level, indicating that the wave function is localized, especially around the Mo atom. The occupied state is considered to be a deep-level feature. It is likely that this deep level functions as a center of recombination for photoinduced e$^-$ and h$^+$ during photocatalysis as it can easily trap carriers generated by photons.[44] This behavior is consistent with findings from previous studies.[45,46] For Mo_V-doped $BiVO_4$, the DOS (Figure 2d) and partial charge density (Figure 3c) are similar to that of F_O-doped $BiVO_4$. This suggests that the Mo atom occupies the position of the V atom and that no impurity state appears in the band gap. This result is consistent with that of our previous calculations.[11]
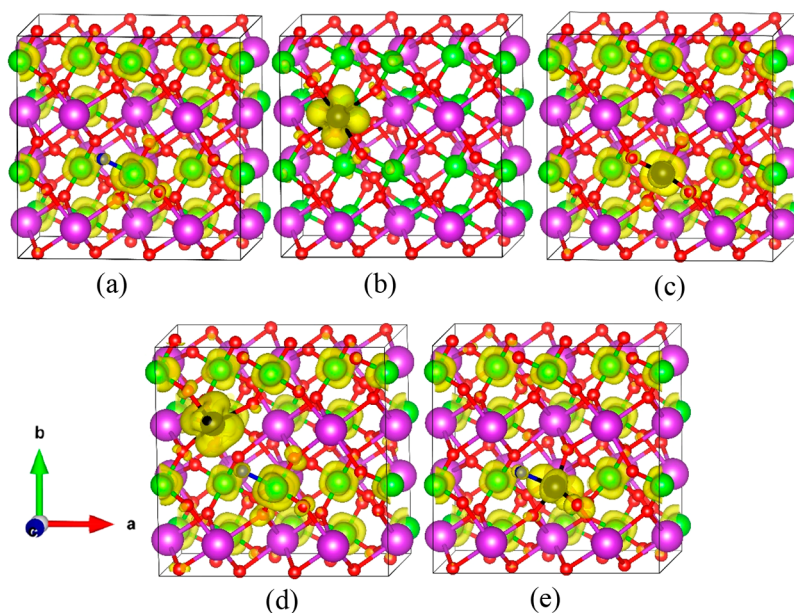
Figure 3. Partial charge density of (a) F_O, (b) Mo_{Bi}, (c) Mo_V, (d) F_OMo_{Bi}, and (e) F_OMo_V-doped $BiVO_4$. The isosurface values are 0.007 e/Å^3. The purple, green, red, black and blue spheres represent Bi, V, O, Mo and F atoms, respectively.
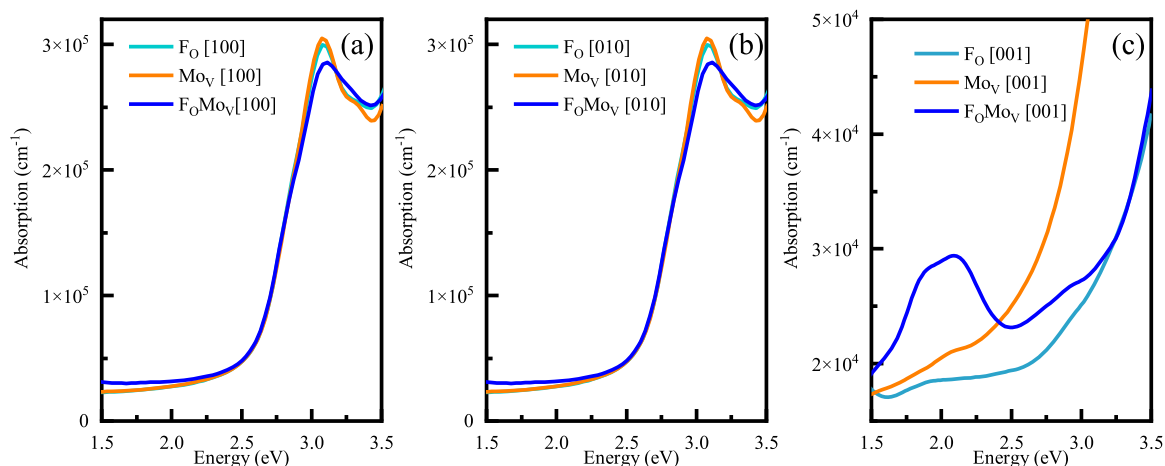

Figure 4. Calculated optical absorption spectra of the F_O-, Mo_V-, and F_OMo_V-doped $BiVO_4$ using the HSE method along with the (a) [100], (b) [010], and (c) [001] directions.

For F_OMo_{Bi}-doped $BiVO_4$, as shown in Figure 2e, the impurity state appears near the bottom of the conduction band edge and would also behave as a donor. A significant reduction in band gap from 2.4 to 2.05 eV is observed. The partial charge density at the CBM (Figure 3d) shows that the wave function is delocalized, implying shallow-level doping. However, as shown in Table 3, the formation energy of F_OMo_{Bi}-doped $BiVO_4$ is the highest under O-poor and O-rich conditions. They are unlikely to form. This indicates that the F_OMo_{Bi} defect in $BiVO_4$ is challenging to form.

Finally, for F_OMo_V-doped $BiVO_4$, as shown in Figure 2f, similar to that of F_OMo_{Bi}-doped $BiVO_4$, the impurity state appears near the bottom of the conduction band edge and would also behave as a donor. Its band gap is 2.25 eV, smaller than that of bulk $BiVO_4$ (2.4 eV). This suggests that visible light absorptions with red shifts of the optical band gap transition are expected compared with undoped $BiVO_4$, which will be discussed in section 3.3. The partial charge density at the CBM (Figure 3e) shows that the wave function is

delocalized, mainly over the V atoms and the Mo atom, which implies shallow-level doping. Thus, this shallow level doping state can promote the charge carrier mobility and photocatalytic activity of FOMoV-doped $BiVO_4$ instead of the deep-level state. More importantly, under O-poor conditions, the formation energy of F_OMoV-doped $BiVO_4$ is the lowest (energetically favorable). This means that shallow-level doping and the lowest formation energy can explain the experimental observation of the F_OMo_V-doped $BiVO_4$ enhanced photocatalytic efficiency.[16]

3.3. Optical Properties. In general, the optical absorption properties of photocatalytic semiconductor materials are closely related to their electronic band structure. It is a significant factor affecting the photocatalytic activity.[47] Due to their large formation energies, the optical absorption properties of Mo_{Bi} and F_OMo_{Bi} are not discussed in this paper. The frequency-dependent absorption coefficients[8,48,49] of the F_O-, Mo_V-, and F_OMo_V-doped $BiVO_4$ can be obtained from the frequency-dependent complex dielectric function:

$$\varepsilon(\omega) = \varepsilon_1(\omega) + i\varepsilon_2(\omega) \tag{8}$$

where $\varepsilon_1(\omega)$ and $\varepsilon_2(\omega)$ are the real and imaginary parts of the dielectric function, respectively, and ω is the phonon energy. The imaginary part $\varepsilon_2(\omega)$ of the dielectric function $\varepsilon(\omega)$ is calculated using the standard formulation:[48]

$$\varepsilon_2(\omega) = \frac{Ve^2}{2\pi\hbar m^2\omega^2}\int d^3\mathbf{k}\sum_{n,n'}|\langle n\mathbf{k}|\mathbf{p}|n'\mathbf{k}\rangle|^2 f_{n\mathbf{k}}(1-f_{n\mathbf{k}'})$$
$$\delta(E_{n\mathbf{k}} - E_{n'\mathbf{k}} - \hbar\omega) \tag{9}$$

where V is the cell volume, $\hbar\omega$ is the incident photon's energy, $\mathbf{p}$ is the momentum operator, $|n\mathbf{k}\rangle$ denotes the electronic state $\mathbf{k}$ in band n, and $f_{n\mathbf{k}}$ is the Fermi occupation function. The real part $\varepsilon_1(\omega)$ is related to $\varepsilon_2(\omega)$ by the Kramer−Krönig transformation. The absorption coefficient $\alpha(\omega)$ can be derived from $\varepsilon_1(\omega)$ and $\varepsilon_2(\omega)$ as follows:[8,49]

$$\alpha(\omega) = \frac{\sqrt{2}\,\omega}{c}[\sqrt{\varepsilon_1^2(\omega) + \varepsilon_2^2(\omega)} - \varepsilon_1(\omega)]^{1/2} \tag{10}$$

The frequency-dependent absorption coefficients along the [100], [010], and [001] directions between 1.5 and 3.5 eV are shown in Figure 4 using the HSE method. It is shown that the doping effect on optical absorption coefficients along the [001] (Figure 4c) is larger than that along [100] and [010] directions (Figure 4a,b). Therefore, we focus on the optical absorption coefficients of the F_O-, Mo_V-, and F_OMo_V-doped BiVO$_4$ along the [001] direction. In Figure 4c, it can be seen that the optical absorption coefficients of the F_OMo_V-doped BiVO$_4$ exhibit one main peak at 2.15 eV. This is due to a transition between nodes occupying the O 2p valence band and states occupying the V 3d and Mo 4d states. Among the main peaks, this one exhibits the most optical absorption (F_O, Mo_V, and F_OMo_V). The results are also consistent with the aforementioned electronic properties. When the energy is greater than 2.4 eV, the optical absorption coefficient for the Mo_V-doped BiVO$_4$ is significantly higher than the F_OMo_V-doped BiVO$_4$. Further, this result shows that the Mo_V-doped BiVO$_4$ highly effectively improves optical absorption in the visible region. This agrees with the experimental[14] and theoretical results.[11]

3.4. Band-Edge Potential. In general, the edge potentials of the conduction band (CB) and valence band (VB) significantly impact photocatalysis. The Mulliken electronegativity theory[50] can predict the CB and VB potentials of bulk BiVO$_4$ and F_O-, Mo_{Bi}-, Mo_V-, F_OMo_{Bi}-, and F_OMo_V-doped BiVO$_4$: $E_{CB} = \chi - E_c - 0.5E_g$ (or $E_{VB} = \chi - E_c + 0.5E_g$), where E_{CB} (E_{VB}) is the conduction (valence) band potential, χ is the absolute electronegativity of bulk BiVO$_4$, and F_O-, Mo_{Bi}-, Mo_V-, F_OMo_{Bi}-, and F_OMo_V-doped BiVO$_4$, E_c is the energy of the free electron in the hydrogen scale (approximately 4.5 eV), and E_g is the band gap energy of the bulk BiVO$_4$, and F_O, Mo_{Bi}, Mo_V, F_OMo_{Bi}, F_OMo_V-doped BiVO$_4$. The band position and photoelectric thresholds for several compounds have been calculated.[9,11,51,52]

Using the calculation method based on our previous literature,[52] we obtained the Mulliken electronegativity (χ) of Bi, V, O, F, and Mo from these data, which are 4.12, 3.60, 7.54, 10.40, and 4.05 eV, respectively.[53,54] The χ value for BiVO$_4$ is 6.04 eV. Therefore, the E_{CB} value of BiVO$_4$ was calculated to be +0.33 eV, and the E_{VB} value was estimated to be +2.73 eV, which agreed well with our previous calculation.[9]

The band-edge positions for bulk BiVO$_4$ and F_O-, Mo_{Bi}-, Mo_V-, F_OMo_{Bi}-, and F_OMo_V-doped BiVO$_4$ are presented in

Figure 5. As shown in Figure 5, the CBM of the F_O-doped BiVO$_4$ is shifted by 0.07 eV toward positive potential, and the
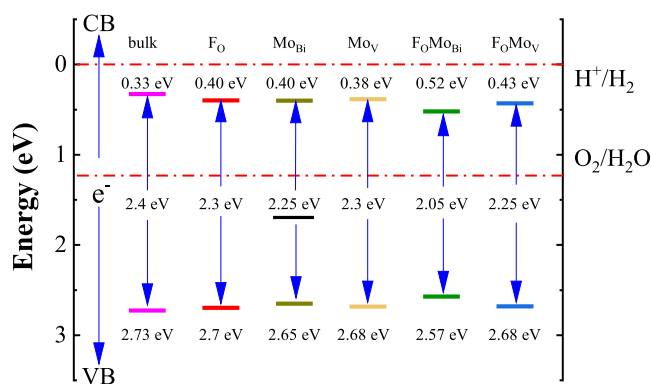

Figure 5. Calculated band gaps and band edge positions of bulk BiVO$_4$, Mo_{Bi}, Mo_V, F_OMo_{Bi}, and F_OMo_V doped using the HSE method. The VBM and CBM values are given concerning the standard redox potentials for water splitting.

VBM is lowered by 0.03 eV relative to that of the bulk BiVO$_4$. Results showed that the oxidizing capacity of the VB and the reducing capacity of the CB both decreased. For Mo_{Bi}-doped BiVO$_4$, the CBM shifts by 0.07 eV toward positive potential, and the VBM is lowered by 0.08 eV compared to the bulk BiVO$_4$, suggesting that both the VB's and CB's reducing capacities will decrease. In addition, one occupied state is introduced into the band gap. Consequently, its photocatalytic activity is negligible owing to its recombination center function. The CBM of Mo_V-doped BiVO$_4$ is shifted by 0.05 eV toward positive potential, and the VBM is lowered by 0.05 eV compared to that of bulk BiVO$_4$. The VB's oxidizing capability and CB's reducing capability are unchanged as a result of this study. CBM and VBM for F_OMo_{Bi}-doped BiVO$_4$ are shifted by 0.19 eV toward positive potential and 0.16 eV toward negative potential, respectively, suggesting that the VB's oxidizing capacity and CB's reducing capacity will both be significantly reduced. The band gap is 2.05 eV, which is the reason. Furthermore, for F_OMo_V-doped BiVO$_4$, the CBM is shifted by 0.10 eV toward positive potential. The VBM is lowered by 0.05 eV, leading to a slight decrease in the oxidizing capacity of the VB and the reducing capacity of the CB. Under visible light irradiation, it exhibits high photocatalytic efficiency and a wide light response range. Its shallow-level doping leads to a small intrinsic band gap and the lowest formation energy.

4. CONCLUSION

This study calculates the formation energy, electronic properties, and photocatalytic activity of F_OMo_V codoped BiVO$_4$ based on the HSE hybrid functional. From the calculated formation energies, we find that Mo atoms prefer to replace V atoms, whereas F atoms prefer to replace O atoms under oxygen-poor conditions. More importantly, BiVO$_4$ doped with F_OMo_V is found to be shallow-level doped, with the occurrence of some continuum states above the conduction band edge. Moreover, F_OMo_V-doped BiVO$_4$ shows absorption stronger than that of pure BiVO$_4$ in the visible spectrum. Finally, based on the band-edge calculation, BiVO$_4$ doped with F_OMo_V retains a high oxidizing capacity. The present results show consistency with the relevant experimental observations.

■ AUTHOR INFORMATION

Corresponding Authors

Jianwen Ding − *School of Physics and Optoelectronic Engineering, Xiangtan University, Xiangtan 411100, China;* Email: jwding@xtu.edu.cn

Wentao Wang − *Guizhou Provincial Key Laboratory of Computational Nano-Material Science, Guizhou Education University, Guiyang 550018, China;* ● orcid.org/0000-0003-4308-3515; Email: wuli8@163.com

Authors

Xia Chen − *School of Physics and Optoelectronic Engineering, Xiangtan University, Xiangtan 411100, China*

Yonggang Wu − *School of Physics and Electronic Science, Guizhou Education University, Guiyang 550018, China*

MingSen Deng − *Guizhou Provincial Key Laboratory of Computational Nano-Material Science, Guizhou Education University, Guiyang 550018, China;* ● orcid.org/0000-0002-3331-3850

Hujun Shen − *Guizhou Provincial Key Laboratory of Computational Nano-Material Science, Guizhou Education University, Guiyang 550018, China;* ● orcid.org/0000-0001-6117-0597

Complete contact information is available at:
https://pubs.acs.org/10.1021/acsomega.2c00382

Author Contributions

[⊥]X.C. and Y.W. contributed equally to this paper.

Notes

The authors declare no competing financial interest.

■ REFERENCES

(1) Kudo, A.; Omori, K.; Kato, H. A Novel Aqueous Process for Preparation of Crystal Form-Controlled and Highly Crystalline BiVO₄ Powder from Layered Vanadates at Room Temperature and Its Photocatalytic and Photophysical Properties. *J. Am. Chem. Soc.* **1999**, *121*, 11459−11467.

(2) Liang, Y.; Tsubota, T.; Mooij, L. P. A.; van de Krol, R. Highly Improved Quantum Efficiencies for Thin Film BiVO₄ Photoanodes. *J. Phys. Chem. C* **2011**, *115*, 17594−17598.

(3) Abdi, F. F.; van de Krol, R. Nature and Light Dependence of Bulk Recombination in Co-Pi-Catalyzed BiVO₄ Photoanodes. *J. Phys. Chem. C* **2012**, *116*, 9398−9404.

(4) Abdi, F. F.; Savenije, T. J.; May, M. M.; Dam, B.; van de Krol, R. The Origin of Slow Carrier Transport in BiVO₄ Thin Film Photoanodes: A Time-Resolved Microwave Conductivity Study. *J. Phys. Chem. Lett.* **2013**, *4*, 2752−2757.

(5) Berglund, S. P.; Flaherty, D. W.; Hahn, N. T.; Bard, A. J.; Mullins, C. B. Photoelectrochemical Oxidation of Water Using Nanostructured BiVO₄ Films. *J. Phys. Chem. C* **2011**, *115*, 3794−3802.

(6) Yu, J.; Kudo, A. Effects of Structural Variation on the Photocatalytic Performance of Hydrothermally Synthesized BiVO₄. *Adv. Funct. Mater.* **2006**, *16*, 2163−2169.

(7) Li, R.; Zhang, F.; Wang, D.; Yang, J.; Li, M.; Zhu, J.; Zhou, X.; Han, H.; Li, C. Spatial Separation of Photogenerated Electrons and Holes among {010} and {110} Crystal Facets of BiVO₄. *Nat. Commun.* **2013**, *4*, 1432.

(8) Zhang, J.; Deng, M.; Yan, Y.; Xiao, T.; Ren, W.; Zhang, P. Tunable Type-II BiVO₄/g-C₃N₄ Nanoheterostructures for Photocatalysis Applications. *Phys. Rev. Appl.* **2019**, *11*, 044052.

(9) Zhang, J.; Ren, F.; Deng, M.; Wang, Y. Enhanced Visible-Light Photocatalytic Activity of a g-C₃N₄/BiVO₄ Nanocomposite: A First-Principles Study. *Phys. Chem. Chem. Phys.* **2015**, *17*, 10218−26.

(10) Zhang, K.; Liu, Y.; Deng, J.; Xie, S.; Zhao, X.; Yang, J.; Han, Z.; Dai, H. Co−Pd/BiVO₄: High-Performance Photocatalysts for the Degradation of Phenol under Visible Light Irradiation. *Appl. Catal., B* **2018**, *224*, 350−359.

(11) Zhang, J.; Deng, M.; Ren, F.; Wu, Y.; Wang, Y. Effects of Mo/W Codoping on the Visible-Light Photocatalytic Activity of Monoclinic BiVO₄ within the GGA + U Framework. *RSC Adv.* **2016**, *6*, 12290−12297.

(12) Zhang, J.; Chen, X.; Deng, M.; Shen, H.; Li, H.; Ding, J. Effects of Native Defects and Cerium Impurity on the Monoclinic BiVO₄ Photocatalyst Obtained Via PBE+U Calculations. *Phys. Chem. Chem. Phys.* **2020**, *22*, 25297−25305.

(13) Luo, W.; Yang, Z.; Li, Z.; Zhang, J.; Liu, J.; Zhao, Z.; Wang, Z.; Yan, S.; Yu, T.; Zou, Z. Solar Hydrogen Generation from Seawater with a Modified BiVO₄ Photoanode. *Energy Environ. Sci.* **2011**, *4*, 4046−4051.

(14) Yang, L.; Xiong, Y.; Guo, W.; Guo, J.; Gao, D.; Zhang, Y.; Xiao, P. Mo ⁶⁺ Doped BiVO₄ with Improved Charge Separation and Oxidation Kinetics for Photoelectrochemical Water Splitting. *Electrochim. Acta* **2017**, *256*, 268−277.

(15) Li, J.-Q.; Guo, Z.-Y.; Liu, H.; Du, J.; Zhu, Z.-F. Two-Step Hydrothermal Process for Synthesis of F-Doped BiVO₄ Spheres with Enhanced Photocatalytic Activity. *J. Alloys Compd.* **2013**, *581*, 40−45.

(16) Rohloff, M.; Anke, B.; Kasian, O.; Zhang, S.; Lerch, M.; Scheu, C.; Fischer, A. Enhanced Photoelectrochemical Water Oxidation Performance by Fluorine Incorporation in BiVO₄ and Mo:BiVO₄ Thin Film Photoanodes. *ACS Appl. Mater. Interfaces* **2019**, *11*, 16430−16442.

(17) Perdew, J. P.; Burke, K.; Ernzerhof, M. Generalized Gradient Approximation Made Simple. *Phys. Rev. Lett.* **1996**, *77*, 3865.

(18) Perdew, J. P.; Wang, Y. Accurate and Simple Analytic Representation of the Electron-Gas Correlation Energy. *Phys. Rev. B* **1992**, *45*, 13244−13249.

(19) Wen, L.; Ding, K.; Huang, S.; Zhang, Y.; Li, Y.; Chen, W. Why Does F-Doping Enhance the Photocatalytic Water-Splitting Performance of M-BiVO₄? − a Density Functional Theory Study. *New J. Chem.* **2017**, *41*, 1094−1102.

(20) Ding, K.; Chen, B.; Fang, Z.; Zhang, Y.; Chen, Z. Why the Photocatalytic Activity of Mo-Doped BiVO₄ Is Enhanced: A Comprehensive Density Functional Study. *Phys. Chem. Chem. Phys.* **2014**, *16*, 13465−76.

(21) Mori-Sanchez, P.; Cohen, A. J.; Yang, W. Localization and Delocalization Errors in Density Functional Theory and Implications for Band-Gap Prediction. *Phys. Rev. Lett.* **2008**, *100*, 146401.

(22) Blochl, P. E. Projector Augmented-Wave Method. *Phys. Rev. B* **1994**, *50*, 17953−17979.

(23) Kresse, G.; Hafner, J. Ab Initio Molecular Dynamics for Liquid Metals. *Phys. Rev. B* **1993**, *47*, 558.

(24) Kresse, G.; Furthmuller, J. Efficient Iterative Schemes for Ab Initio Total-Energy Calculations Using a Plane-Wave Basis Set. *Phys. Rev. B* **1996**, *54*, 11169.

(25) Monkhorst, H. J.; Pack, J. D. Special Points for Brillouin-Zone Integrations. *Phys. Rev. B* **1976**, *13*, 5188.

(26) Mohn, C. E.; Stølen, S. Influence of the Stereochemically Active Bismuth Lone Pair Structure on Ferroelectricity and Photocalytic Activity of Aurivillius Phase Bi₂WO₆. *Phys. Rev. B* **2011**, *83*, 014103.

(27) Walsh, A.; Watson, G. W.; Payne, D. J.; Edgell, R. G.; Guo, J.; Glans, P.-A.; Learmonth, T.; Smith, K. E. Electronic Structure of

The α and δ phases of Bi_2O_3: A Combined ab Initio and X-Ray Spectroscopy Study. *Phys. Rev. B* **2006**, *73*, 235104.

(28) Heyd, J.; Scuseria, G. E.; Ernzerhof, M. Hybrid Unctionals Based on a Screened Coulomb Potential. *J. Chem. Phys.* **2003**, *118*, 8207–8215.

(29) Krukau, A. V.; Vydrov, O. A.; Izmaylov, A. F.; Scuseria, G. E. Influence of the Exchange Screening Parameter on the Performance of Screened Hybrid Functionals. *J. Chem. Phys.* **2006**, *125*, 224106–224112.

(30) Cooper, J. K.; Gul, S.; Toma, F. M.; Chen, L.; Liu, Y.-S.; Guo, J.; Ager, J. W.; Yano, J.; Sharp, I. D. Indirect Bandgap and Optical Properties of Monoclinic Bismuth Vanadate. *J. Phys. Chem. C* **2015**, *119*, 2969–2974.

(31) Yin, W. J.; Wei, S. H.; Al-Jassim, M. M.; Turner, J.; Yan, Y. F. Doping Properties of Monoclinic $BiVO_4$ Studied by First-Principles Density-Functional Theory. *Phys. Rev. B* **2011**, *83*, 155102.

(32) Wang, J.; Ma, A.; Li, Z.; Jiang, J.; Chen, J.; Zou, Z. Effects of Mg–Zr Codoping on the Photoelectrochemical Properties of a Ta_3n_5 Semiconductor: A Theoretical Insight. *J. Mater. Chem. A* **2017**, *5*, 6966–6973.

(33) Chase, M. W. *NIST-Janaf Thermochemical Tables*; American Institute of Physics, 1998.

(34) Sun, S. P.; Zhu, J. L.; Gu, S.; Li, X. P.; Lei, W. N.; Jiang, Y.; Yi, D. Q.; Chen, G. H. First Principles Investigation of the Surface Stability and Equilibrium Morphology of MoO_3. *Appl. Surf. Sci.* **2019**, *467–468*, 753–759.

(35) Hovick, J. W.; Bartell, L. S. Inference of Temperatures of Cold Crystalline Clusters from Lattice Constants Via Grüneisen's Relation. An Electron Diffraction Study. *J. Mol. Struct.* **1995**, *346*, 231–238.

(36) Yang, Z.; Wang, X.; Pei, Y.; Liu, L.; Su, X. First Principles Study on the Structural, Magnetic and Electronic Properties of Te-Doped BiF_3. *Comput. Mater. Sci.* **2012**, *60*, 212–216.

(37) Williamson, R. F.; Boo, W. O. J. Lower Valence Fluorides of Vanadium. 4. The Rutile-Like Compounds VF_2, $MgVF_4$, $Li_{0.50}VF_3$, and Opaque VF^{2+}.Delta. *Inorg. Chem.* **1980**, *19*, 31–34.

(38) Edwards, A. J.; Jones, G. R. Fluoride Crystal Structures. Part Vii. Vanadium Pentafluoride. *Journal of the Chemical Society A: Inorganic, Physical, Theoretical* **1969**, *1*, 1651–1654.

(39) Park, Y.; McDonald, K. J.; Choi, K. S. Progress in Bismuth Vanadate Photoanodes for Use in Solar Water Oxidation. *Chem. Soc. Rev.* **2013**, *42*, 2321–2337.

(40) Sleight, A. W.; Chen, H. y.; Ferretti, A.; Cox, D. E. Crystal Growth and Structure of $BiVO_4$. *Mater. Res. Bull.* **1979**, *14*, 1571–1581.

(41) Jiang, H.; Dai, H.; Deng, J.; Liu, Y.; Zhang, L.; Ji, K. Porous F-Doped $BiVO_4$: Synthesis and Enhanced Photocatalytic Performance for the Degradation of Phenol under Visible-Light Illumination. *Solid State Sci.* **2013**, *17*, 21–27.

(42) Rohloff, M.; Anke, B.; Wiedemann, D.; Ulpe, A. C.; Kasian, O.; Zhang, S.; Scheu, C.; Bredow, T.; Lerch, M.; Fischer, A. Synthesis and Doping Strategies to Improve the Photoelectrochemical Water Oxidation Activity of $BiVO_4$ Photoanodes. *Z. Phys. Chem.* **2020**, *234*, 655–682.

(43) Luo, W.; Wang, J.; Zhao, X.; Zhao, Z.; Li, Z.; Zou, Z. Formation Energy and Photoelectrochemical Properties of $BiVO_4$ after Doping at Bi^{3+} or V^{5+} Sites with Higher Valence Metal Ions. *Phys. Chem. Chem. Phys.* **2013**, *15*, 1006–13.

(44) Ma, X.; Lu, B.; Li, D.; Shi, R.; Pan, C.; Zhu, Y. Origin of Photocatalytic Activation of Silver Orthophosphate from First-Principles. *J. Phys. Chem. C* **2011**, *115*, 4680–4687.

(45) Zhang, H.; Liu, L.; Zhou, Z. First-Principles Studies on Facet-Dependent Photocatalytic Properties of Bismuth Oxyhalides (BiOXs). *RSC Adv.* **2012**, *2*, 9224.

(46) Dai, W. W.; Zhao, Z. Y. Structural and Electronic Properties of Low-Index Stoichiometric BiOI Surfaces. *Mater. Chem. Phys.* **2017**, *193*, 164–176.

(47) Sun, L.; Qi, Y.; Jia, C. J.; Jin, Z.; Fan, W. Enhanced Visible-Light Photocatalytic Activity of g-C_3N_4/Zn_2GeO_4 Heterojunctions with Effective Interfaces Based on Band Match. *Nanoscale* **2014**, *6*, 2649–2659.

(48) Zhang, J.; Cao, J. X.; Chen, X.; Ding, J. W.; Zhang, P.; Ren, W. Diamond Nanowires with Nitrogen Vacancy under a Transverse Electric Field. *Phys. Rev. B* **2015**, *91*, 045417.

(49) Saha, S.; Sinha, T. P.; Mookerjee, A. Electronic Structure, Chemical Bonding, and Optical Properties of Paraelectric $BaTiO_3$. *Phys. Rev. B* **2000**, *62*, 8828.

(50) Butler, M. A.; Ginley, D. S. Prediction of Flatband Potentials at Semiconductor-Electrolyte Interfaces from Atomic Electronegativities. *J. Electrochem. Soc.* **1978**, *125*, 228.

(51) Lim, Y. K.; Keong Koh, E. W.; Zhang, Y.-W.; Pan, H. Ab Initio Design of GaN-Based Photocatalyst: ZnO-Codoped GaN Nanotubes. *J. Power Sources* **2013**, *232*, 323–331.

(52) Zhang, J.; Deng, P.; Deng, M.; Shen, H.; Feng, Z.; Li, H. Hybrid Density Functional Theory Study of Native Defects and Nonmetal (C, N, S, and P) Doping in a Bi_2WO_6 Photocatalyst. *ACS Omega* **2020**, *5*, 29081–29091.

(53) Andersen, T.; Haugen, H. K.; Hotop, H. Binding Energies in Atomic Negative Ions: Iii. *J. Phys. Chem. Ref. Data* **1999**, *28*, 1511–1533.

(54) Kittel, C. *Introduction to Solid State Physics*, 8th ed.; Wiley, 2005.